2026 IEEE International Conference on Robotics and Automation (ICRA 2026)
June 1-5, 2026. Vienna, Austria

Iterative Learning-based Centre-of-Mass Impedance Control for Articulated-Soft Humanoid Robots

Yibin Wang[1], Lin Zhou, Sacha Morris, Shan Luo, Emmanouil Spyrakos-Papastavridis

***Abstract*— Achieving safe and robust interaction in articulated-soft humanoid robots (ASRs) remains a major challenge due to their compliant joints, high degree of freedom, and highly nonlinear coupled dynamics, which makes them especially sensitive to external disturbances. This paper presents a novel contact-force-based iterative learning center-of-mass (CoM) impedance control framework (CF-IL-CIC) specifically designed to enhance disturbance robustness in floating-base ASRs. The key idea is to iteratively derive a time-series gross force compensation term from zero moment point (ZMP) tracking errors of previous trials, using a proportional-derivative (PD)-type update rule in simulation. This compensation is integrated with a contact-force-based CoM impedance controller to improve push recovery without requiring precise dynamic models or heavy online optimization. The approach is accompanied by mathematical proof of divergent component of motion (DCM) error convergence, ensuring theoretical stability guarantees. The proposed method is validated through both dynamic simulations and real-robot experiments on the compliant humanoid BRUCE, demonstrating significant improvements in external impact rejection and recovery stability compared to baseline controllers.**

I. INTRODUCTION

Bipedal locomotion greatly enhances the mobility and dexterity of a legged robot, allowing it to operate effectively in human-designed environments. However, articulated-soft humanoid robots (ASRs), which integrate passive compliance through series elastic actuation, face unique challenges compared to rigid humanoids. Their flexible joints and underactuated structures lead to highly nonlinear, strongly coupled dynamics, making balance recovery under physical interaction particularly difficult. These difficulties are most apparent during push recovery, where both stability and safe energy dissipation must be achieved simultaneously.

Despite the complexity of such high-dimensional systems, the essence of walking can often be captured by low-dimensional dynamics. To exploit this property, simplified models and hierarchical control frameworks have been developed, where low-dimensional models guide high-level planning, while whole-body models map planned motions to joint-level torques or positions [1]. The zero moment point (ZMP), first introduced in [2], became a fundamental stability criterion, requiring the ZMP to remain within the support polygon to prevent falling. Building on this, the linear inverted pendulum model (LIPM) [3] enabled efficient gait planning, while the capture point [4] and its generalization, the divergent component of motion (DCM) [5], further decomposed CoM dynamics for robust balance control. The DCM was later extended to 3D for continuous force-based gait planning [6]. Whole-body control (WBC) frameworks [1], [7] subsequently mapped these task-space trajectories into high-dimensional joint torques for real robots.

All authors are with the Centre for Robotics Research, Department of Engineering, Faculty of Natural, Mathematical and Engineering Sciences, King's College London, Strand, London, WC2R 2LS, U.K. {yibin.1.wang, lin.zhou, sacha.morris, shan.luo, emmanouil.spyrakos}@kcl.ac.uk

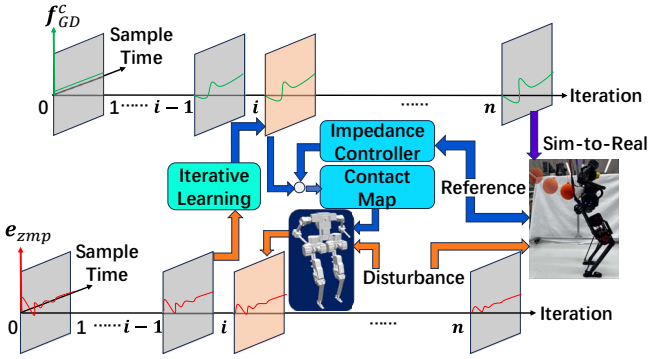

Fig. 1: Overview of the control strategy workflow. The CoM impedance controller computes the gross desired force from reference, combined with the gross desired force compensation term f^c_{GD}, and sends it to the contact map and robot dynamics (more details are shown in Fig. 2). f^c_{GD} is updated iteratively based on the ZMP error e_{zmp} caused by disturbance. The final f^c_{GD} is transferred to hardware for real-world execution with the same reference and disturbance.

While these approaches improved locomotion performance, bipedal robots operating in unstructured human environments face stricter requirements for stability, safety, and disturbance rejection. Control strategies such as contact force-based control [8], [9] explicitly regulate interaction forces and are critical for physical human-robot interaction. On the hardware side, flexible joints and series elastic actuators (SEAs) [10]–[12] have been introduced to reduce interface stiffness, leading to ASRs. These designs improve impact resilience and safety but demand more sophisticated controllers [13]. Impedance control has been widely adopted to regulate the virtual mechanical impedance of the legs [14], allowing safe adaptation to uneven terrain and sudden changes [15], [16]. Variable impedance control (VIC) extends this idea by adjusting impedance online [17]–[21]. Adaptive VIC for minimizing leg-body force tracking error [22] and optimization-based tuning of stiffness and damping [23] further enhance interaction performance. However, increasing stiffness can compromise passivity and stability [24], [25]. Passive preservation schemes [26] and model-free floating-base VIC [13] have been proposed to mitigate these issues, yet stability under strong disturbances remains

challenging. Recent studies also explore DCM-based feedback strategies for stabilizing compliant floating-base robots under external disturbances [27].

Iterative learning control (ILC) improves performance for repetitive tasks by learning from previous executions [28]. Unlike neural networks or adaptive control, ILC directly adjusts the control input and converges within a few iterations [29], [30]. ILC has been applied to industrial robots [31], [32], underwater robots [33], and bipedal locomotion [34]–[36]. Existing works include ZMP compensation for walking stability [35], [36] and robust motion learning under flexible drives [37], [38]. However, most ILC studies focus on rigid-body humanoids and joint-space implementations, which scale poorly to high-DoF ASRs and rarely address external, unstructured disturbances [39].

To address these limitations, we propose a novel contact-force-based iterative learning CoM impedance control framework (CF-IL-CIC) specifically designed for articulated-soft humanoid robots. Unlike prior joint-space ILC methods, our controller directly learns a gross force compensation term in Cartesian space from ZMP tracking errors, significantly reducing model dependency and computational cost, as illustrated in Fig. 1. This design fully leverages the compliance of ASRs, enabling enhanced push recovery without requiring precise dynamics or online optimization. Furthermore, the stability of the proposed framework is reinforced through the integration of power-shaping-signal control (PSC), which proves the convergence of the DCM error.

Key contributions include:

1) A novel ZMP-error-driven iterative learning scheme integrated with a contact-force-based impedance controller, explicitly addressing the challenges of flexible-joint humanoids and improving disturbance rejection through repeated impact experience;
2) Incorporation of PSC to provide a theoretical guarantee of CoM error convergence and system stability;
3) Hardware validation on the compliant humanoid BRUCE, demonstrating successful sim-to-real transfer and superior robustness compared to baseline controllers.

The remainder of the paper is organized as follows: Section II reviews the balancing criteria and contact force modeling for articulated-soft humanoids. Section III introduces the proposed iterative learning strategy in detail. Section IV presents simulation and sim-to-real experimental validations using the BRUCE platform. Section V concludes with discussions and future research directions.

II. Contact Force-Based Impedance Control

A. Divergent Component of Motion

Under the constant CoM height assumption commonly adopted in humanoid locomotion, centroidal motion can be approximated by the Linear Inverted Pendulum Model (LIPM) [40]–[42]. Following the capture point and divergent component of motion (DCM) formulation in [5], the CoM motion can be decomposed into stable and unstable components. The DCM of $\boldsymbol{p}_{dcm}$ is defined as:

$$\boldsymbol{p}_{dcm} = \boldsymbol{c} + b\dot{\boldsymbol{c}} \tag{1}$$

where $\boldsymbol{c} = \begin{bmatrix} x, y, z \end{bmatrix}^\top$ and $\dot{\boldsymbol{c}} = \begin{bmatrix} \dot{x}, \dot{y}, \dot{z} \end{bmatrix}^\top$ denote the position and velocity of the CoM, and b is the time-constant of the DCM dynamics. By derivating Eq. (1), we can find the dynamics of the CoM $\dot{\boldsymbol{c}}$:

$$\dot{\boldsymbol{c}} = -\frac{1}{b}(\boldsymbol{c} - \boldsymbol{p}_{dcm}) \tag{2}$$

Eq. (2) shows that the CoM has a stable first-order dynamics when $b > 0$. By differentiating Eq. (1) and inserting Eq. (2), the dynamics of the DCM $\dot{\boldsymbol{p}}_{dcm}$ could be expressed as:

$$\dot{\boldsymbol{p}}_{dcm} = -\frac{1}{b}\boldsymbol{c} + \frac{1}{b}\boldsymbol{p}_{\boldsymbol{dcm}} + \frac{b}{m}\boldsymbol{F} \tag{3}$$

This means that the total force $\boldsymbol{F}$ influences the DCM dynamics directly.

B. Contact Force Map

For a floating-base robot to remain statically or dynamically stable, it must generate a sufficient gross applied force on the ground. In legged robots, this force is distributed across multiple contact points, where each point k produces a desired contact force vector $\boldsymbol{f}_{k_d} = \begin{bmatrix} f_{k_{d_x}}, f_{k_{d_y}}, f_{k_{d_z}} \end{bmatrix}^\top$. Stacking all individual vectors forms the total contact-force vector $\boldsymbol{f}_{cd} = \begin{bmatrix} f_{1_x}, f_{1_y}, f_{1_z}, \ldots, f_{k_z} \end{bmatrix}^\top \in \mathbb{R}^{3k\times 1}$; for instance, a biped with four contact points has $k = 4$, yielding $\boldsymbol{f}_{cd} \in \mathbb{R}^{12\times 1}$. Now, the approach for designing a balancing controller is to distribute the desired contact force $\boldsymbol{f}_{cd}$. to all the contact points, such that they guarantee a gross desired $\boldsymbol{f}_{GD}$ on the robot [43], i.e.,

$$\boldsymbol{f}_{GD} = \boldsymbol{\Phi}_{\mathrm{c}}\boldsymbol{f}_{cd} \tag{4}$$

$$\boldsymbol{\Phi}_{\mathrm{c}} = \begin{bmatrix} I_{3\times 3} & \ldots & I_{3\times 3} \\ \hat{\boldsymbol{\phi}}_1 & \ldots & \hat{\boldsymbol{\phi}}_k \end{bmatrix} \tag{5}$$

where $\boldsymbol{\Phi}_c \in \mathbb{R}^{6\times 3k}$ is the contact map matrix, $\hat{\boldsymbol{\phi}}$ is the cross-product matrix corresponding to the relative position vector from CoM to contact location $\boldsymbol{\phi} = \begin{bmatrix} x_p, y_p, z_p \end{bmatrix}^\top$, given by:

$$\hat{\boldsymbol{\phi}} = \begin{bmatrix} 0 & -z_p & y_p \\ z_p & 0 & -x_p \\ -y_p & x_p & 0 \end{bmatrix} \tag{6}$$

C. Model of a Flexible-Joint Floating-base Robot with Multiple Contacts

To account for joint elasticity, an n-coordinate actuator model is added to the initial representation [44], which produces:

$$\mathbf{M}_{\mathrm{fb}}\ddot{\boldsymbol{c}} + \boldsymbol{G}_{fb} = \boldsymbol{f}_G \tag{7}$$

$$\mathbf{M}(\boldsymbol{q})\ddot{\boldsymbol{q}} + \mathbf{N}\dot{\boldsymbol{q}} + \mathbf{C}(\boldsymbol{q}, \dot{\boldsymbol{q}})\dot{\boldsymbol{q}} + \mathbf{K}(\boldsymbol{q} - \boldsymbol{\theta}) = \mathbf{J}_{\mathrm{G}}^\top(\boldsymbol{q})\boldsymbol{f}_G \tag{8}$$

$$\mathbf{J}\ddot{\boldsymbol{\theta}} + \mathbf{D}\dot{\boldsymbol{\theta}} + \mathbf{K}(\boldsymbol{\theta} - \boldsymbol{q}) = \boldsymbol{\tau}_m \tag{9}$$

where $\boldsymbol{q} \in \mathbb{R}^n$ and $\boldsymbol{\theta} \in \mathbb{R}^n$ denote the joint/base-attitude and motor position vectors. $\mathbf{M}(\boldsymbol{q}), \mathbf{N}, \mathbf{C}$, and $\mathbf{K} \in \mathbb{R}^{n\times n}$ denote the inertia, damping, Coriolis/centrifugal, and passive stiffness matrices. $\mathbf{M}_{\text{fb}} = \text{diag}(m, m, m)$ is the floating-base mass matrix, and $\boldsymbol{G}_{\text{fb}} = \mathbf{M}_{\text{fb}}\boldsymbol{g}$ is the gravity term. $\boldsymbol{f}_G \in \mathbb{R}^6$ denotes the gross contact wrench, and $\mathbf{J}_G \in \mathbb{R}^{6\times n}$ the contact Jacobian. $\boldsymbol{\tau}_m \in \mathbb{R}^n$ is the motor input torque, whereas $\mathbf{J}, \mathbf{D} \in \mathbb{R}^{n\times n}$ are the motor inertia and damping matrices. Under this formulation, the robot contact forces and moments are not directly actuated through $\boldsymbol{\tau}_m$.

D. Contact-force-based CoM Impedance Controller

The DCM time constant can be substituted by $b = \sqrt{\frac{z_{vc}}{g}}$. The desired CoM position c_d can be obtained by initially setting a desired DCM $\boldsymbol{p}_{dcm_d}$ by:

$$\boldsymbol{c}_d = \boldsymbol{p}_{dcm_d} - \sqrt{\frac{z_{vc}}{g}}\,\dot{\boldsymbol{c}} \tag{10}$$

where z_{vc} is the desired height of CoM. Then the velocity $\dot{\boldsymbol{c}}_d$ of the CoM can also be calculated. As a result, the position error $\boldsymbol{c}_E = \boldsymbol{c}_d - \boldsymbol{c}$ and the velocity error $\dot{\boldsymbol{c}}_E = \dot{\boldsymbol{c}}_d - \dot{\boldsymbol{c}}$ can be obtained. The gross desired force $\boldsymbol{f}_{GD}$ of the robot is then calculated by combining with the gravity compensation $\boldsymbol{G}_{comp}$:

$$\boldsymbol{f}_{GD} = \mathbf{K}_{\text{p}}\boldsymbol{c}_E + \mathbf{K}_{\text{d}}\dot{\boldsymbol{c}}_E + \boldsymbol{G}_{comp} \tag{11}$$

where $\mathbf{K}_{\text{p}}$ and $\mathbf{K}_{\text{d}}$ are the stiffness and damping gain matrices, respectively, and $\boldsymbol{G}_{comp}$ is the gravitational compensation term, decoupling equilibrium maintenance from the impedance regulation of dynamic tracking errors. The corresponding contact forces can be computed via Eq. (4):

$$\boldsymbol{f}_{cd} = \boldsymbol{\Phi}_{\text{c}}^{\#}\boldsymbol{f}_{GD} \tag{12}$$

with the pseudoinverse of the contact map given as:

$$\boldsymbol{\Phi}_{\text{c}}^{\#} = \boldsymbol{\Phi}_{\text{c}}^{\top}(\boldsymbol{\Phi}_{\text{c}}\,\boldsymbol{\Phi}_{\text{c}}^{\top})^{-1} \tag{13}$$

The mapping of the wrench to joint:

$$\boldsymbol{\tau}_m = -\mathbf{J}_{\text{c}}^{\top}\boldsymbol{f}_{cd} \tag{14}$$

where $\mathbf{J}_{\text{c}} = \left[\mathbf{J}_{\text{c1}}, \ldots, \mathbf{J}_{\text{ci}}\right]^{\top} \in \mathbb{R}^{3i\times n}$ is the contact-point-to-CoM Jacobian, with $\mathbf{J}_{\text{ci}} \in \mathbb{R}^{n\times 3}$ denoting the Jacobian corresponding to the ith contact point. Four contact points are considered: left toe, left heel, right toe, and right heel.

III. Iterative Learning Based COM Impedance Control for Bipedal Robots

A. Iterative Learning Law based on Contact-Aware Balance Indicator: Zero-Moment Point

Considering the robot multi-body dynamics and contact model [45], the general ZMP is defined by:

$$\begin{bmatrix} p_{zmp_x} \\ p_{zmp_y} \end{bmatrix} = \frac{1}{\sum_{i=1}^{k} f_{i_z}} \begin{bmatrix} \sum_{i=1}^{k} f_{i_z} x_i \\ \sum_{i=1}^{k} f_{i_z} y_i \end{bmatrix}. \tag{15}$$

where (p_{zmp_x}, p_{zmp_y}) is ZMP position, (x_i, y_i) indicate the position of each contact points, f_{i_z} represent the vertical component of corresponding contact forces.

Due to calibration issues with the IMU-based CoM estimation of the robotic experiment platform, tracking performance is suboptimal, causing inaccuracies in the CoM and DCM trajectories during dynamic operations. Therefore, iterative updates are based on the error of the physically defined ZMP—computed from contact points and forces—instead of the CoM or DCM trajectories.

B. PD-type Iterative Learning-based CoM Impedance Controller

The iterative learning strategy is obtained by adjusting the predefined control input with a corrective term that linearly depends on the tracking error, a widely used ILC learning algorithm [28] is:

$$u_{j+1}(k) = Q(a)[u_j(k) + L(a)e_j(k+1)] \tag{16}$$

$$e_j(k) = y_d(k) - y_j(k) \tag{17}$$

where k is the time index, j is the iteration index, y_j is the output, u_j is the control input, e_j is the error signal, a is the forward time-shift operator $ax(k) \equiv x(k+1)$. And the dynamics $Q(a)$ and $L(a)$ denote the Q-filter, and learning, functions, respectively. The logic of ILC is shown in Fig 5.

Currently, four main types of ILC algorithms exist. Among them, the PD-type learning function is the most widely adopted due to its simple tuning and minimal modeling requirements. [28]. A discrete-time, PD-type learning function can be written as:

$$u_{j+1}(k) = u_j(k) + P_l e_j(k+1) + D_l[e_j(k+1) - e_j(k)] \tag{18}$$

where P_l is the proportional gain and D_l is the derivative gain. The system with the PD-type ILC algorithm is asymptotically stable if and only if $|1 - (P_l + D_l)p_1| < 1$. When p_1 is known, it is always possible to find P_l and D_l such that the system is asymptotically stable. Monotonic convergence, however, is not always possible in PD-type learning algorithm, except when the iteration is sufficiently short [28].

The system with the PD-type Iterative Learning Control (ILC) scheme is illustrated in Fig. 2. According to the PD-ILC framework, the control input u_j and the error signal e_j must be properly defined for the bipedal robot system. Due to the system complexity, multiple reference signals may exist at different levels. Although the CoM or DCM positions can serve as primary performance indicators for stability and trajectory tracking, the ZMP error is adopted as the learning error signal e_j, denoted as $\boldsymbol{e}_{zmp_j}$, which is a three-dimensional vector in Cartesian space. For consistency, the control input u_j is also defined in Cartesian space. Thus, the gross desired force $\boldsymbol{f}_{GD}$ is considered as the control-related variable. However, since $\boldsymbol{f}_{GD}$ is not directly generated by error feedback in the bipedal robot system, the compensation term of the gross desired force, $\boldsymbol{f}_{GD}^{c}$, is

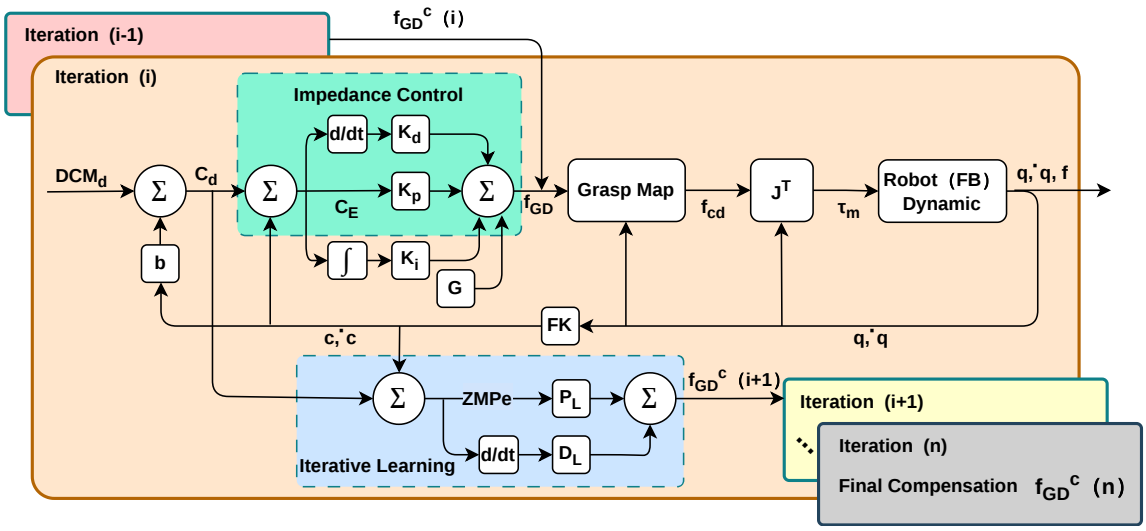

Fig. 2: Block diagram of the CF-IL-CIC. The desired DCM generates the CoM reference through the LIPM model, which is then sent to the CoM impedance controller to compute the gross desired force $\boldsymbol{f}_{GD}$. Via the mapping matrix and contact Jacobian, $\boldsymbol{f}_{GD}$ is mapped to the contact forces and corresponding joint torques for robot motion control. To improve tracking performance, an iterative learning mechanism updates the input force: at iteration i, $\boldsymbol{f}_{GD}$ is combined with the compensation term $\boldsymbol{f}_{GD}^{c}$ from iteration $i-1$ to produce $\widehat{\boldsymbol{f}}_{GD}$. The compensation term is computed from the ZMP error $\boldsymbol{e}_{\text{zmp}}$ and applied in iteration $i+1$.

selected as the control input u_j. The corresponding ILC update law is expressed as follows:

$$\boldsymbol{f}_{GD_{j+1}}^{c}(k) = \begin{cases} \boldsymbol{f}_{GD_j}^{c}(k) + P_l\, \boldsymbol{e}_{zmp_j}(k+1) \\ \quad \text{if } \boldsymbol{F}_{impact} > \mathbf{0}, \\ \boldsymbol{f}_{GD_j}^{c}(k) + D_l[\boldsymbol{e}_{zmp_j}(k+1) - e_{zmp_j}] \\ \quad \text{if } \boldsymbol{F}_{impact} \leq \mathbf{0}. \end{cases} \tag{19}$$

where $\boldsymbol{f}_{GD}^{c}$ denotes the compensation term of $\boldsymbol{f}_{GD}$, while $\boldsymbol{F}_{\text{impact}}$ represents the impact force introduced as an experimental disturbance. When the system is subjected to a short-duration impact force $\boldsymbol{F}_{\text{impact}}$, the compensation is primarily produced by the proportional gain P_l to counteract the increase in position error. In the presence of oscillations, the compensatory effect is mainly dominated by the derivative gain D_l to damp the oscillations of the system. By modifying Eq. (11), the compensated optimal gross desired force $\widehat{\boldsymbol{f}}_{GD}$ can be obtained. Meanwhile, the integral matrix $\mathbf{K}_{\text{i}}$ is incorporated to suppress steady-state error.

$$\widehat{\boldsymbol{f}}_{GD} = \boldsymbol{f}_{GD} + \boldsymbol{f}_{GD}^{c} \tag{20}$$

$$\boldsymbol{f}_{GD} = \mathbf{K}_{\text{p}}\, \boldsymbol{c}_E + \mathbf{K}_{\text{d}}\, \dot{\boldsymbol{c}}_E + \mathbf{K}_{\text{i}} \int_0^t \boldsymbol{c}_E + \boldsymbol{G}_{comp} \tag{21}$$

by substituting Eq. (12) into Eq. (14) and considering Eq. (20), the new control law can be obtained as follows:

$$\boldsymbol{\tau}_m = -\mathbf{J}_{\text{c}}^{\top}\, \boldsymbol{\Phi}_{\text{c}}^{\#}\, \widehat{\boldsymbol{f}}_{GD} \tag{22}$$

C. Stability of CF-IL-CIC

The stiffness-increasing phases can potentially impinge on stability and/or passivity, which is similar to that modified the controller by introducing an external compensation as a result of their energy-injecting nature as mentioned above [25]. [13] [26] have proposed stability-preserving schemes for VIC of flexible-joint robots, through utilisation of Power-Shaping Control (PSC), which guarantees stable and passive VIC of floating-base systems with contacts as well [46]. Unlike PSC-based approaches that require the time derivative of the active stiffness terms, the proposed method avoids such computation, thereby simplifying the subsequent stability analysis. The stability of the CF-IL-CIC, which is proposed in this paper, can be proved in a manner analogous to the method in [47], [48]. By substituting Eqs. (20) and (21) into Eq. (22), the proposed control law that includes PSC terms could be obtained as follows:

$$\begin{aligned} \boldsymbol{\tau}_m = &-\mathbf{J}_{\text{c}}^{\top}\, \boldsymbol{\Phi}_{\text{c}}^{\#}\, \widehat{\boldsymbol{f}}_{GD} + \mathbf{K}(\boldsymbol{\theta} - \boldsymbol{q}) - \mathbf{K}_{\text{D}_\text{M}} \dot{\boldsymbol{\theta}} - p_{vn} \mathbf{K}_{\text{D}_\text{J}} \dot{\boldsymbol{q}} \\ &+ p_{v0} \left(\mathbf{J} \ddot{\boldsymbol{\theta}} + \mathbf{J}_{\text{c}}^{\top}\, \boldsymbol{\Phi}_{\text{c}}^{\#}\, \widehat{\boldsymbol{f}}_{GD} \right) + \mathbf{S}_{\text{P}} \boldsymbol{I}_R \tau_f \end{aligned} \tag{23}$$

where $\mathbf{K}_{\text{D}_\text{M}}, \mathbf{K}_{\text{D}_\text{J}}$ are diagonal, positive definite matrices, $\mathbf{S}_{\text{P}} = diag(\dot{\boldsymbol{\theta}})^{\#}$, $\boldsymbol{I}_R = \left[1, ..., 1_n\right]^{\top} \cdot rank(\mathbf{S}_{\text{P}})^{\#}$, $p_{v0} = 1 - \dot{\boldsymbol{\theta}}^{\top} \mathbf{S}_{\text{P}} \boldsymbol{I}_R$. $p_{vn} = 1$ when $\dot{\boldsymbol{\theta}} = \mathbf{0}$, and $p_{vn} = 0$ either when $\dot{\boldsymbol{\theta}} \neq \mathbf{0}$ or $\dot{\boldsymbol{q}}_{fb}^{\top} = \left[\dot{\boldsymbol{c}}^{\top}, \dot{\boldsymbol{q}}^{\top}, \dot{\boldsymbol{\theta}}^{\top}\right] \equiv \mathbf{0}$ and $\boldsymbol{p}_{dcm_E} \equiv \mathbf{0}$. $\mathbf{S}_{\text{P}} \boldsymbol{I}_R \tau_f$ can be made arbitrarily small, in order to guarantee feasible signals at all times, by following the approach in [19], [44], [47]. τ_f is the power-shaping signal given as:

$$\begin{aligned} \tau_f = &\dot{\boldsymbol{c}}^{\top} (\boldsymbol{G}_{fb} - \boldsymbol{f}_G) - \dot{\boldsymbol{p}}_{dcm_E}^{\top} (p_{vs} \mathbf{K}_{\text{CM}}) \boldsymbol{p}_{dcm_E} \\ &- \dot{\boldsymbol{q}}^{\top} \mathbf{J}_{\text{G}}^{\top}(\boldsymbol{q}) \boldsymbol{f}_G + \dot{\boldsymbol{\theta}}^{\top} \mathbf{J}_{\text{c}}^{\top}\, \boldsymbol{\Phi}_{\text{c}}^{\#}\, \widehat{\boldsymbol{f}}_{GD} + \dot{\boldsymbol{q}}^{\top} \mathbf{K}(\boldsymbol{q} - \boldsymbol{\theta}) \\ &- \boldsymbol{p}_{dcm_E}^{\top} \mathbf{K}_{\text{CD}} \boldsymbol{p}_{dcm_E} \end{aligned} \tag{24}$$

where $p_{vs} = (1 - p_{vn})$. $\mathbf{K}_{\text{CM}}, \mathbf{K}_{\text{CD}} \in \mathbb{R}^{m \times m}$ are user-defined positive definite, diagonal matrices.

The motor-side closed-loop dynamics and the corresponding Lyapunov function are presented below:

$$\mathbf{J}\ddot{\boldsymbol{\theta}} = -\mathbf{J}_{\mathrm{c}}^{\top}\boldsymbol{\Phi}_{\mathrm{c}}^{\#}\widehat{\boldsymbol{f}}_{GD} - \mathbf{K}_{\mathrm{D_M}}\dot{\boldsymbol{\theta}} - p_{vn}\mathbf{K}_{\mathrm{D_I}}\dot{\boldsymbol{q}} + p_{v0}\Big(\mathbf{J}\ddot{\boldsymbol{\theta}} + \mathbf{J}_{\mathrm{c}}^{\top}\boldsymbol{\Phi}_{\mathrm{c}}^{\#}\widehat{\boldsymbol{f}}_{GD}\Big) + \mathbf{S}_{\mathrm{P}}\boldsymbol{I}_R\tau_f - \mathbf{D}\dot{\boldsymbol{\theta}} \tag{25}$$

$$V = \frac{1}{2}\dot{\boldsymbol{q}}_{fb}^{\top}\mathbf{M}_{\mathrm{fc}}\dot{\boldsymbol{q}}_{fb} + \frac{1}{2}\boldsymbol{p}_{dcm_E}^{\top}(p_{vs}\mathbf{K}_{\mathrm{CM}})\boldsymbol{p}_{dcm_E} \tag{26}$$

where $\boldsymbol{q}_{fb}^{\top} = \left[\boldsymbol{c}^{\top}, \boldsymbol{q}^{\top}, \boldsymbol{\theta}^{\top}\right]$. It is worth noting that the particular structure of the closed-loop dynamics guarantees that $\dot{\boldsymbol{q}} = \mathbf{0}$ when $\dot{\boldsymbol{\theta}} = \mathbf{0}$. One may then proceed by following the New Invariance Principle to prove closed-loop stability based on this Lyapunov function and its derivative [49]. The derivative of the above Lyapunov function can be simplified, based on the fact that $\dot{\boldsymbol{\theta}}^{\top}\mathbf{S}_{\mathrm{P}}\boldsymbol{I}_R = 1$ when $\dot{\boldsymbol{\theta}} \neq 0$ and that $\dot{\boldsymbol{q}}_{fb}^{\top}(\dot{\mathbf{M}}_{\mathrm{fc}} - 2\mathbf{C})\dot{\boldsymbol{q}}_{fb} = 0$, thus yielding:

$$\dot{V} = -\dot{\boldsymbol{q}}_{fb}^{\top} diag(\mathbf{0}, \mathbf{N}, \mathbf{D} + \mathbf{K}_{\mathrm{D_M}})\dot{\boldsymbol{q}}_{fb} - \boldsymbol{p}_{dcm_E}^{\top}\mathbf{K}_{\mathrm{CD}}\boldsymbol{p}_{dcm_E} \tag{27}$$

which is negative semi-definite. Since $\mathbf{N}, \mathbf{D}$ are positive definite, based on the New Invariance Principle [49], it can be concluded that $[\dot{\boldsymbol{c}}^{\top}, \dot{\boldsymbol{q}}^{\top}] \equiv \mathbf{0}$ and $\boldsymbol{p}_{dcm_E} \equiv \mathbf{0}$, given that it is always possible, based on the above derivative expression, to define a function $W > \dot{V}$ (away from equilibria). Hence, this satisfies the conditions outlined in [49], enabling one to state that $[\dot{\boldsymbol{c}}^{\top}, \dot{\boldsymbol{q}}^{\top}] \equiv \mathbf{0}$ and $\boldsymbol{p}_{dcm_E} \equiv \mathbf{0}$. By substituting Eq. (10) into Eq. (2), the following relationship is obtained:

$$\boldsymbol{c}_E = \boldsymbol{p}_{dcm_E} \tag{28}$$

where $[\dot{\boldsymbol{c}}^{\top}, \dot{\boldsymbol{q}}^{\top}] \equiv \mathbf{0}$ and $\boldsymbol{p}_{dcm_E} \equiv \mathbf{0}$ implies, based on $\dot{\boldsymbol{c}} + \mathbf{J}_{\mathrm{G}}(\boldsymbol{q})\dot{\boldsymbol{q}} = \mathbf{0}$, that $\dot{\boldsymbol{c}} = \mathbf{0}$; hence, $\boldsymbol{p}_{dcm_E} = \boldsymbol{c}_E = \mathbf{0}$. Then, using $\dot{\boldsymbol{c}}_d = \dot{\boldsymbol{c}} - \sqrt{\frac{g}{z_{vc}}}\boldsymbol{c}_E$, it can be said that $\boldsymbol{c}_E = \mathbf{0}$ guarantees that $\dot{\boldsymbol{c}}_E = \mathbf{0}$. Hence, $\boldsymbol{c}_E$ and $\boldsymbol{p}_{dcm_E}$ converge to zero asymptotically, provided that $\mathbf{J}_{\mathrm{c}}$ is away from singularities

IV. Iterative Learning-Based Bipedal Robot Simulations and Hardware Experiments

ASRs, equipped with impedance controllers, can automatically adjust stiffness during interaction with the environment or humans, thereby enhancing task performance and interactive safety [50]. Without such compliant structures, complex interactive tasks would be extremely difficult to accomplish. Prior works [51], [52] introduced dual-jointed musculoskeletal structures to reduce control bandwidth requirements while enabling joint coordination and energy transfer, which improves efficiency, compliance, and resistance to impacts [53]. The Bipedal Robot Unit with Compliance Enhanced (BRUCE) [12], employing a cable-driven differential pulley system, achieves further compliance while maintaining lightweight design.

In this work, the proposed learning control framework is validated on BRUCE (Fig. 3(b)), a 70 cm, 4.8 kg bipedal robot with human-like proportions. BRUCE has two 5-DoF legs and two 3-DoF arms; in the conducted experiments, only the 12 leg DoFs are torque-controlled, while the upper body's joints are controlled to constant positions. Each leg includes a spherical hip, a 1-DoF knee, and a 1-DoF ankle. The feet provide line contact and are equipped with ground contact sensors. Simulations are conducted in Gazebo using the BRUCE model (Fig. 3(a)).

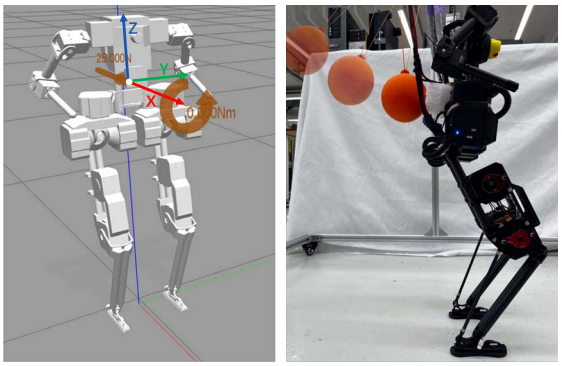

(a) (b)

Fig. 3: BRUCE robot model and experimental setup. (a) Simulation model implemented in Gazebo, illustrating the robot's kinematic structure and dynamic interaction; (b) Physical hardware setup demonstrating the experimental scenario for validation.

A. Simulation Training Environment and Experimental Setup

The proposed learning control framework was evaluated in both dynamic simulation and real-robot experiments. The evaluation focuses on disturbances along the sagittal (x) direction, as it corresponds to the most restrictive dimension of the support polygon during standing and therefore determines the minimum stability margin. A static balancing simulation with external impact was conducted to validate the effectiveness of the contact force iterative learning impedance controller. In the simulation, the robot model was initialized for 8 s to ensure ZMP stability before impact. The control loop was executed at 1 kHz. An external force $\boldsymbol{F}_{impact} = [25, 0, 0]$ N was applied for 0.008 s ($I = 0.2$Ns) in each iteration to simulate external disturbances. The simulation was terminated once the compensation signals converged or the optimization criterion was satisfied.

For the hardware experiment, an elastic ball pendulum with 92.5g was employed to generate impacts, as shown in Fig. 3(b). The release height H of the pendulum was setting as 80cm ($\Delta H = 15$cm) to match the impulse magnitude used in the simulation. Both controllers use identical impedance gains $\mathbf{K}_{\mathrm{p}} = \mathrm{diag}(100, 150, 1000)$ and $\mathbf{K}_{\mathrm{d}} = \mathrm{diag}(1, 1, 5)$; the proposed method augments the nominal controller only through an additive iterative feedforward term, leaving the feedback dynamics unchanged.

B. Iterative Learning Simulation Results

Since this experiment primarily focuses on the effect of external impacts, the compensation signal $\boldsymbol{f}_{GD}^{c}$ is activated when an impact occurs to mitigate its influence. The initial value of $\boldsymbol{f}_{GD}^{c}$ is set to zero and gradually converges through iterative updates. By incorporating $\boldsymbol{f}_{GD}^{c}$ into the impedance controller, the CoM error peak in the final iteration is significantly reduced compared to the initial iteration, as shown in Fig. 4(c). Specifically, the peak CoM error along the X-axis decreased from 18.37 mm to 15.44 mm (red and

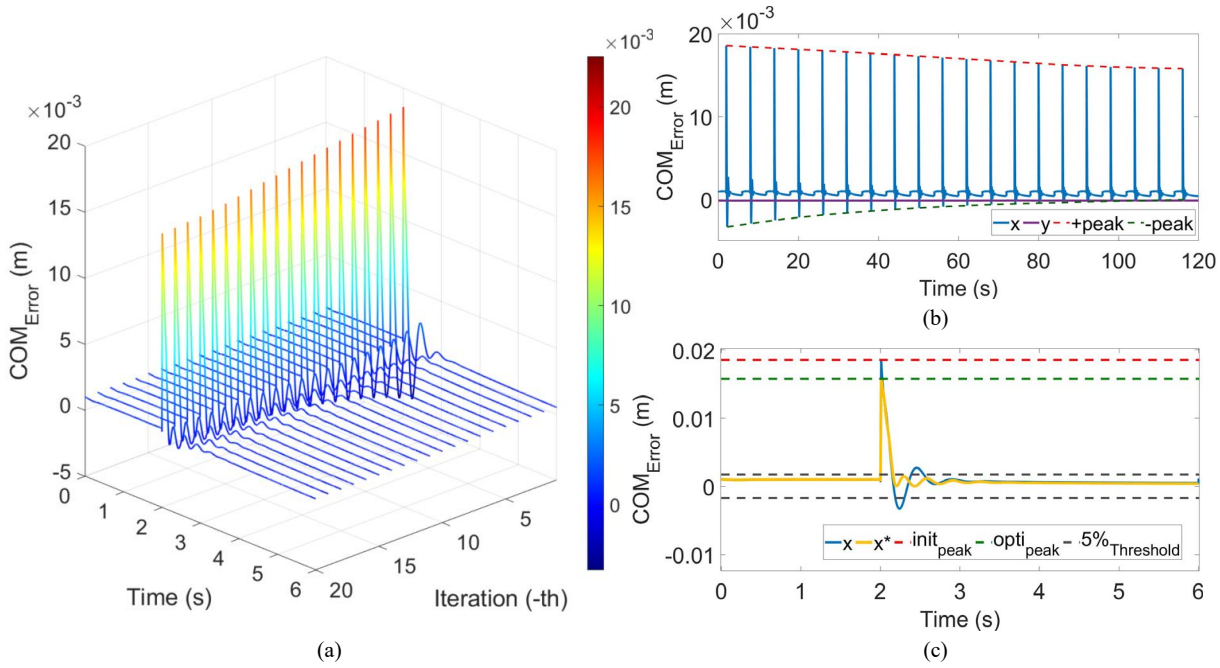

Fig. 4: Variation of CoM error during 20 iterative processes in simulation. (a) Three-dimensional visualization of CoM error evolution over 20 iterations; (b) CoM error trajectory across 20 iterations within a single process, where peaks correspond to error variations caused by experimental impacts. The red and green dashed lines indicate fitted curves for positive and negative peak values, respectively; (c) Comparison of CoM error before compensation (1st iteration) and after compensation (20th iteration). The blue curve represents initial CoM error, while the yellow curve shows optimized CoM error after iterative control. The red and green dashed lines denote respective peak values, and the gray dashed line indicates a $\pm 5\%$ settling band relative to the peak value.

green dashed lines in Fig. 4(c)) after eliminating the steady-state error of 0.99 mm, resulting in a 16.85% improvement in disturbance rejection performance. Furthermore, the settling time is reduced by approximately 0.3s.

C. Physical BRUCE Balancing using Iterative Learning Controller Experiment Results

The simulation-derived compensation signal $\boldsymbol{f}_{GD}^{c}$ (Fig. 5(a)) was transferred to the BRUCE robot (sim-to-real) to validate the iterative learning impedance control strategy on hardware. This approach was adopted due to hardware safety constraints and the difficulty of reproducing consistent disturbances.

Since the impact and compensation signal in simulation were indexed by sample time, the hardware controller requires a compensation signal activator for disturbance detection. The trigger condition is $|\dot{\boldsymbol{c}}_E| > 0.006\,\mathrm{m/s}$, upon which the impedance controller switches to execute $\boldsymbol{f}_{GD}^{c}$.

In the hardware experiment, repeated pendulum impacts were applied. Since IMU estimation and joint motor feedback were unreliable, the ZMP error was used to evaluate controller performance, as shown in Fig. 5(c). To account for variations in steady-state error and impact intervals, the Root Mean Square (RMS) of every 10 peaks over 1000 samples was adopted as the performance metric.

The algorithm is benchmarked against the manufacturer-provided controller integrated in the default BRUCE platform, serving as a rigorously validated hardware baseline. Three controllers are evaluated: the quadratic programming-based contact force solver (QP-solver, BRUCE's default), the basic contact force-based CoM impedance controller (CF-CIC), and the proposed CF-IL-CIC. The results show that CF-CIC improves steady-state recovery and disturbance rejection by 34.82% over the QP-solver, while CF-IL-CIC further improves performance by 25.49% compared with CF-CIC. Since the proposed method operates in task space, direct comparison with joint-space optimization approaches is not meaningful; therefore, disturbance recovery metrics are reported.

V. Conclusion And Future Work

This paper presented a novel contact-force-based iterative learning CoM impedance control framework (CF-IL-CIC) for articulated-soft humanoid robots, addressing the challenge of improving disturbance robustness without relying on precise dynamic models or heavy online optimization. A time-series gross force compensation term was iteratively updated from previous ZMP tracking errors using a PD-type learning rule and integrated into a contact-force-based impedance controller via a contact-point grasp map.In addition, the framework incorporates PSC to ensure theoretical stability by regulating the system's energy behavior and guaranteeing the convergence of DCM errors. Experiments on the compliant bipedal robot BRUCE demonstrated that the proposed method substantially reduces ZMP error and improves recovery stability under external impacts, outperforming both the baseline CF-CIC and the default QP-solver controller. Future work will extend the framework to stochastic and unstructured disturbances, enable real-time online learning

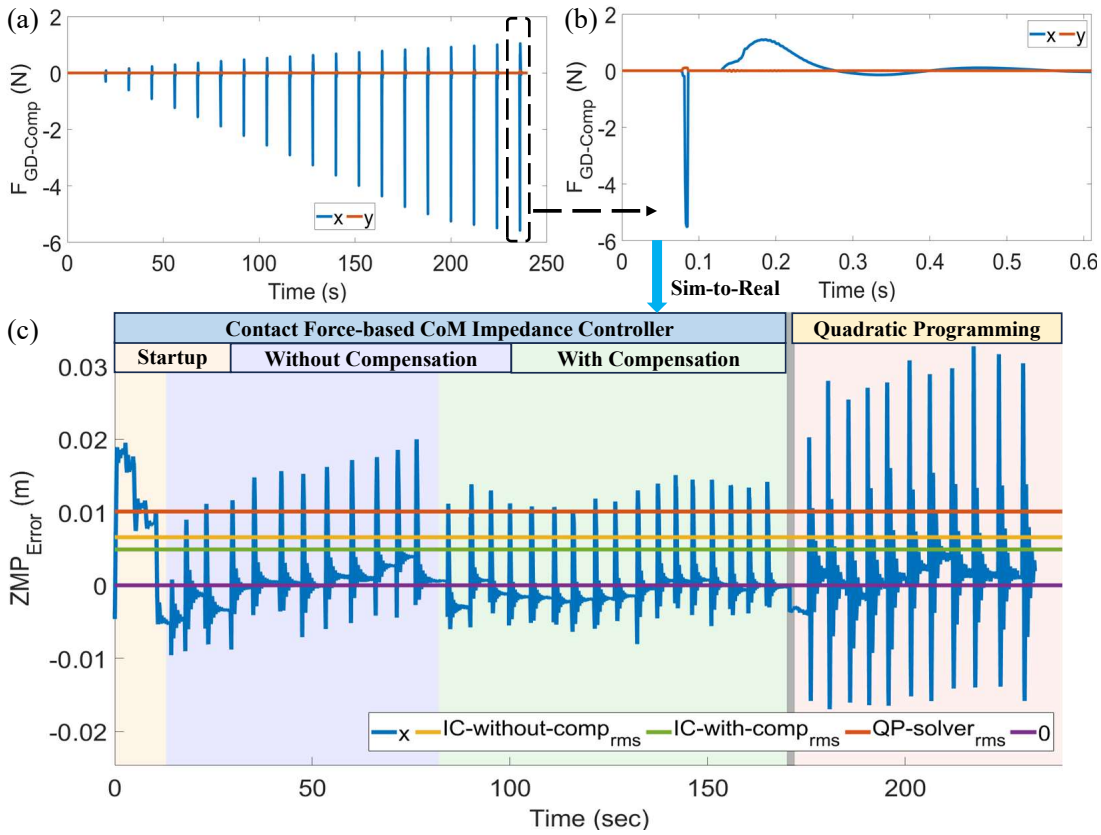

Fig. 5: The ZMP error of robot on hardware experiment. (a) compensation signal $\boldsymbol{f}^c_{GD}$ over one iterative process, showing 20 iterations. (b) The zoomed-in view of last iteration $\boldsymbol{f}^c_{GD}$, which be implemented on hardware. (c) ZMP error of the robot in the hardware experiment along the x-axis. The yellow area highlights errors due to startup disturbances. The purple region shows the controller without compensation, while the green region corresponds to the activation of the iterative learning compensation $\boldsymbol{f}^c_{GD}$.The pink area represents the controller that calculates contact forces using the default quadratic programming solver, rather than the impedance controller. RMS values of the ZMP error are indicated as follows: red line – quadratic programming (10.11mm), yellow line – without compensation (6.59mm), green line – with compensation (4.91mm), and purple line – baseline (0mm).

on hardware, and integrate it with advanced whole-body control for safer physical human–robot interaction. We will also compare it with model-free and disturbance-observer-based balancing methods, analyze convergence of the iterative learning update, and evaluate each controller component's contribution to the performance gains.

References

[1] L. Sentis and O. Khatib, "A whole-body control framework for humanoids operating in human environments," in *Proceedings 2006 IEEE International Conference on Robotics and Automation, 2006. ICRA 2006.*, 2006, pp. 2641–2648.

[2] M. Vukobratović and B. Borovac, "Zero-moment point—thirty five years of its life," *International journal of humanoid robotics*, vol. 1, no. 01, pp. 157–173, 2004.

[3] S. Kajita, F. Kanehiro, K. Kaneko, K. Yokoi, and H. Hirukawa, "The 3d linear inverted pendulum mode: A simple modeling for a biped walking pattern generation," in *Proceedings 2001 IEEE/RSJ International Conference on Intelligent Robots and Systems. Expanding the Societal Role of Robotics in the the Next Millennium (Cat. No.01CH37180)*, vol. 1, 2001, 239–246 vol.1.

[4] J. Pratt, J. Carff, S. Drakunov, and A. Goswami, "Capture point: A step toward humanoid push recovery," in *2006 6th IEEE-RAS International Conference on Humanoid Robots*, 2006, pp. 200–207.

[5] T. Takenaka, T. Matsumoto, and T. Yoshiike, "Real time motion generation and control for biped robot -1st report: Walking gait pattern generation-," in *2009 IEEE/RSJ International Conference on Intelligent Robots and Systems*, 2009, pp. 1084–1091.

[6] J. Englsberger, C. Ott, and A. Albu-Schäffer, "Three-dimensional bipedal walking control based on divergent component of motion," *Ieee transactions on robotics*, vol. 31, no. 2, pp. 355–368, 2015.

[7] O. Khatib, L. Sentis, and J.-H. Park, "A unified framework for whole-body humanoid robot control with multiple constraints and contacts," in *European Robotics Symposium 2008*, H. Bruyninckx, L. Přeučil, and M. Kulich, Eds. Berlin, Heidelberg: Springer Berlin Heidelberg, 2008, pp. 303–312.

[8] J. Park and O. Khatib, "A haptic teleoperation approach based on contact force control," *The International Journal of Robotics Research*, vol. 25, no. 5-6, pp. 575–591, 2006.

[9] F. Chen, H. Zhao, D. Li, L. Chen, C. Tan, and H. Ding, "Contact force control and vibration suppression in robotic polishing with a smart end effector," *Robotics and Computer-Integrated Manufacturing*, vol. 57, pp. 391–403, 2019.

[10] S. Eppinger and W. Seering, "Three dynamic problems in robot force control," *IEEE Transactions on Robotics and Automation*, vol. 8, no. 6, pp. 751–758, 1992.

[11] S. Eppinger and W. Seering, "Understanding bandwidth limitations in robot force control," in *Proceedings. 1987 IEEE international conference on robotics and automation*, vol. 4, 1987, pp. 904–909.

[12] Y. Liu, J. Shen, J. Zhang, X. Zhang, T. Zhu, and D. Hong, "Design and control of a miniature bipedal robot with proprioceptive actuation for dynamic behaviors," in *2022 International Conference on Robotics and Automation (ICRA)*, 2022, pp. 8547–8553.

[13] E. Spyrakos-Papastavridis and J. S. Dai, "Flexible-joint humanoid balancing augmentation via full-state feedback variable impedance control," *Journal of Mechanisms and Robotics*, vol. 13, no. 2, p. 021 014, 2021.

[14] G. A. Pratt and M. M. Williamson, "Series elastic actuators," in *Proceedings 1995 IEEE/RSJ international conference on intelligent*

robots and systems. Human robot interaction and cooperative robots, vol. 1, 1995, pp. 399–406.

[15] B. G. Son, J. T. Kim, and J. H. Park, "Impedance control for biped robot walking on uneven terrain," in *2009 IEEE International Conference on Robotics and Biomimetics (ROBIO)*, 2009, pp. 239–244.

[16] E. Spyrakos-Papastavridis, G. A. Medrano-Cerda, N. G. Tsagarakis, J. S. Dai, and D. G. Caldwell, "A compliant humanoid walking strategy based on the switching of state feedback gravity compensation controllers," in *2013 IEEE/RSJ International Conference on Intelligent Robots and Systems*, 2013, pp. 3630–3636.

[17] F. J. Abu-Dakka and M. Saveriano, "Variable impedance control and learning—a review," *Frontiers in Robotics and AI*, vol. 7, p. 590 681, 2020.

[18] C. Zeng, Y. Li, J. Guo, Z. Huang, N. Wang, and C. Yang, "A unified parametric representation for robotic compliant skills with adaptation of impedance and force," *IEEE/ASME Transactions on Mechatronics*, vol. 27, no. 2, pp. 623–633, 2021.

[19] E. Spyrakos-Papastavridis and J. S. Dai, "A variable impedance scheme based on power-shaping signals and partial knowledge of link-side dynamics for flexible-joint robot interaction and tracking control," *IEEE/ASME Transactions on Mechatronics*, vol. 29, no. 1, pp. 588–601, 2023.

[20] E. S. Papastavridis, N. Kashiri, J. Lee, N. G. Tsagarakis, and D. G. Caldwell, "Online impedance parameter tuning for compliant biped balancing," in *Online Impedance Parameter Tuning for Compliant Biped Balancing*, 2015.

[21] E. Spyrakos-Papastavridis, N. Kashiri, P. R. Childs, and N. G. Tsagarakis, "Online impedance regulation techniques for compliant humanoid balancing," *Robotics and Autonomous Systems*, vol. 104, pp. 85–98, 2018.

[22] K. Xu, S. Wang, B. Yue, *et al.*, "Adaptive impedance control with variable target stiffness for wheel-legged robot on complex unknown terrain," *Mechatronics*, vol. 69, p. 102 388, 2020.

[23] M. J. Pollayil, F. Angelini, G. Xin, *et al.*, "Choosing stiffness and damping for optimal impedance planning," *IEEE Transactions on Robotics*, vol. 39, no. 2, pp. 1281–1300, 2022.

[24] K. Kronander and A. Billard, "Stability considerations for variable impedance control," *IEEE Transactions on Robotics*, vol. 32, no. 5, pp. 1298–1305, 2016.

[25] F. Ferraguti, N. Preda, A. Manurung, *et al.*, "An energy tank-based interactive control architecture for autonomous and teleoperated robotic surgery," *IEEE Transactions on Robotics*, vol. 31, no. 5, pp. 1073–1088, 2015.

[26] E. Spyrakos-Papastavridis, P. R. Childs, and J. S. Dai, "Passivity preservation for variable impedance control of compliant robots," *IEEE/ASME Transactions on Mechatronics*, vol. 25, no. 5, pp. 2342–2353, 2019.

[27] E. Spyrakos-Papastavridis, Y. Wang, L. Zhou, K. Wang, and J. S. Dai, "Stability-guaranteed control via divergent-component-of-motion feedback for force-based balancing in articulated-soft floating-base robots," *IEEE Robotics and Automation Letters*, 2025.

[28] D. A. Bristow, M. Tharayil, and A. G. Alleyne, "A survey of iterative learning control," *IEEE control systems magazine*, vol. 26, no. 3, pp. 96–114, 2006.

[29] K. L. Moore, *Iterative learning control for deterministic systems*, 1993.

[30] K. J. Hunt, D. Sbarbaro, R Żbikowski, and P. J. Gawthrop, "Neural networks for control systems—a survey," *Automatica*, vol. 28, no. 6, pp. 1083–1112, 1992.

[31] M. Norrlof, "An adaptive iterative learning control algorithm with experiments on an industrial robot," *IEEE Transactions on robotics and automation*, vol. 18, no. 2, pp. 245–251, 2002.

[32] D.-I. Kim and S. Kim, "An iterative learning control method with application for cnc machine tools," *IEEE Transactions on Industry Applications*, vol. 32, no. 1, pp. 66–72, 1996.

[33] S. Kawamura and N. Sakagami, "Analysis on dynamics of underwater robot manipulators based on iterative learning control and time-scale transformation," in *Proceedings 2002 IEEE International Conference on Robotics and Automation (Cat. No. 02CH37292)*, vol. 2, 2002, pp. 1088–1094.

[34] L. Kwek, E. Wong, C. K. Loo, and M. Rao, "Application of active force control and iterative learning in a 5-link biped robot," *Journal of Intelligent and Robotic Systems*, vol. 37, no. 2, pp. 143–162, 2003.

[35] Q.-Z. Zhang, C. Chee-Meng, Y.-L. Zhou, Q.-L. Zhao, and P. Li, "Iterative learning control for biped walking," in *2010 IEEE International Conference on Mechatronics and Automation*, 2010, pp. 237–241.

[36] K. Hu, C. Ott, and D. Lee, "Online iterative learning control of zero-moment point for biped walking stabilization," in *2015 IEEE International Conference on Robotics and Automation (ICRA)*, 2015, pp. 5127–5133.

[37] M. Pierallini, F. Angelini, R. Mengacci, A. Palleschi, A. Bicchi, and M. Garabini, "Trajectory tracking of a one-link flexible arm via iterative learning control," in *2020 IEEE/RSJ International Conference on Intelligent Robots and Systems (IROS)*, 2020, pp. 7579–7586.

[38] J. Ding, M. A. van Löben Sels, F. Angelini, J. Kober, and C. Della Santina, "Robust jumping with an articulated soft quadruped via trajectory optimization and iterative learning," *IEEE Robotics and Automation Letters*, vol. 9, no. 1, pp. 255–262, 2023.

[39] R. Mengacci, F. Angelini, M. G. Catalano, G. Grioli, A. Bicchi, and M. Garabini, "On the motion/stiffness decoupling property of articulated soft robots with application to model-free torque iterative learning control," *The International Journal of Robotics Research*, vol. 40, no. 1, pp. 348–374, 2021.

[40] S. Dubowsky and E. Papadopoulos, "The kinematics, dynamics, and control of free-flying and free-floating space robotic systems," *IEEE Transactions on robotics and automation*, vol. 9, no. 5, pp. 531–543, 2002.

[41] T. Sugihara, Y. Nakamura, and H. Inoue, "Real-time humanoid motion generation through zmp manipulation based on inverted pendulum control," in *Proceedings 2002 IEEE International Conference on Robotics and Automation (Cat. No. 02CH37292)*, vol. 2, 2002, pp. 1404–1409.

[42] S. Kajita, F. Kanehiro, K. Kaneko, *et al.*, "Biped walking pattern generation by using preview control of zero-moment point," in *2003 IEEE international conference on robotics and automation (Cat. No. 03CH37422)*, vol. 2, 2003, pp. 1620–1626.

[43] C. Ott, M. A. Roa, and G. Hirzinger, "Posture and balance control for biped robots based on contact force optimization," in *2011 11th IEEE-RAS International Conference on Humanoid Robots*, 2011, pp. 26–33.

[44] E. Spyrakos-Papastavridis and J. S. Dai, "Stable flexible-joint floating-base robot balancing and locomotion via variable impedance control," *IEEE Transactions on Industrial Electronics*, vol. 70, no. 3, pp. 2748–2758, 2022.

[45] S.-H. Hyon, J. G. Hale, and G. Cheng, "Full-body compliant human–humanoid interaction: Balancing in the presence of unknown external forces," *IEEE transactions on robotics*, vol. 23, no. 5, pp. 884–898, 2007.

[46] E. Spyrakos-Papastavridis and J. S. Dai, "A model-free solution for stable balancing and locomotion of floating-base legged systems," in *2020 IEEE/RSJ International Conference on Intelligent Robots and Systems (IROS)*, 2020, pp. 3816–3822.

[47] E. Spyrakos-Papastavridis, Z. Fu, and J. S. Dai, "Power-shaping model-based control with feedback deactivation for flexible-joint robot interaction," *IEEE Robotics and Automation Letters*, vol. 7, no. 2, pp. 4566–4573, 2022.

[48] E. Spyrakos-Papastavridis, K. Wang, and J. S. Dai, "Integral action in variable impedance control of articulated-soft robots," *IEEE Transactions on Automation Science and Engineering*, 2025.

[49] I. Barkana, "Defending the beauty of the invariance principle," *International Journal of Control*, vol. 87, no. 1, pp. 186–206, 2014.

[50] M. Stölzle, S. S. Baberwal, D. Rus, S. Coyle, and C. Della Santina, "Guiding soft robots with motor-imagery brain signals and impedance control," in *2024 IEEE 7th International Conference on Soft Robotics (RoboSoft)*, 2024, pp. 276–283.

[51] W. Roozing, Z. Ren, and N. G. Tsagarakis, "An efficient leg with series–parallel and biarticular compliant actuation: Design optimization, modeling, and control of the eleg," *The International Journal of Robotics Research*, vol. 40, no. 1, pp. 37–54, 2021.

[52] C Schumacher, M Sharbafi, A Seyfarth, and C Rode, "Biarticular muscles in light of template models, experiments and robotics: A review," *Journal of the Royal Society Interface*, vol. 17, no. 163, p. 20 180 413, 2020.

[53] G. Ficht and S. Behnke, "Bipedal humanoid hardware design: A technology review," *Current Robotics Reports*, vol. 2, no. 2, pp. 201–210, 2021.